


# First results of the SA Agulhas II mobile mini-neutron monitor

## Instrumental characterization and environmental sensitivity

Du Toit Strauss <sup>1</sup>, Frederic Effenberger <sup>2</sup>, Stefan Lotz <sup>3</sup>, Konstantin Herbst <sup>4</sup>, Helena Krüger<sup>1</sup>, Corrie Diedericks<sup>1</sup>

### Correspondence

- 1 Center for Space Research, North-West University, Potchefstroom, South Africa, [dutoit.strauss@nwu.ac.za](mailto:dutoit.strauss@nwu.ac.za), [helenakruger6@gmail.com](mailto:helenakruger6@gmail.com), [27863840@nwu.ac.za](mailto:27863840@nwu.ac.za)
  - 2 Institut für Theoretische Physik, Lehrstuhl IV: Plasma-Astroteilchenphysik, Ruhr-Universität Bochum, Germany, [fe@tp4.rub.de](mailto:fe@tp4.rub.de)
  - 3 South African National Space Agency, Hermanus, South Africa, [slotz@sansa.org.za](mailto:slotz@sansa.org.za)
  - 4 Extraterrestrial Physics, Institute of Experimental and Applied Physics, Kiel University, Germany, [herbst@physik.uni-kiel.de](mailto:herbst@physik.uni-kiel.de)
- 

### Keywords

neutron monitor; cosmic rays; heliosphere; modulation; instrumentation

### Abstract

We present the first results of a new redesigned version of the mini-neutron monitor installed on the South African Research vessel, the SA Agulhas II. Measurements taken from the 2019/2020 relief voyages are presented. We show that the instrument is very sensitive to temperature variations when the ambient temperature is below 3°C. This is believed to be an instrumental effect. Additionally, we show the presence of high-frequency interference in the calculated waiting time distributions when the vessel reaches polar latitudes. We show that these periodic variations are only present in the intensity of secondary atmospheric particles and most likely related to the operation of the vessel's ice radar. We are currently looking at moving the instrument to a more suitable location on board the SA Agulhas II where we will hopefully be able to operate the instrument in a continuous fashion for several years to come.

## 1. Introduction

Neutron monitors (NMs) have been used for more than 70 years to monitor the indirect flux of cosmic rays in the near-Earth environment. Primary cosmic ray particles that enter the Earth's atmosphere produce showers of secondary particles (including protons, neutrons, and other particles and sub-atomic particles).



**Fig. 1:** The left panel shows the SA Agulhas II unloading supplies in Antarctica with the location of the mini-NM circled. The right panel shows the monitor, emphasizing the newly installed vibration dampeners.

These secondary particles are registered on the ground level by the NM, so that the NM count rate  $N$  can be expressed as

$$N(P_c, t) = \sum_i \int_{P_c}^{\infty} j_i(P, t) Y_i(P, t, \dots) dP$$

where  $P_c$  is the cut-off rigidity (minimum rigidity particle that can reach the detector due to deflection by the geomagnetic field),  $j_i$  is the primary cosmic ray flux at the top of the atmosphere,  $i$  represents the particle distribution under consideration, and  $Y$  is the so-called yield function that represents the response of the instrument on the unit flux of primary cosmic rays with rigidity  $P$ , including atmospheric and instrumental effects. The latter therefore depends on various parameters that are unique to each monitor (Caballero-Lopez 2016; Clem and Dorman 2000). The rigidity dependence of  $Y$  can, however, be calculated experimentally by placing the monitor (or at least some tubes making up the large monitors) on a ship that crosses multiple latitudes (and thereby sampling different regions of  $P$ ) in a relatively short time (e.g. Caballero-Lopez and Moraal 2012, amongst many others). This is referred to as a latitude scan and has been carried out many times in the past by various groups.

The mini-NM is a small and compact version of the standard NM (Simpson 2000; Bütikofer 2018), originally envisioned to serve as a *calibration* NM (Moraal et al. 2001; Krüger et al. 2003). However, under the right conditions, it was realized that the mini-NM could supplement the existing network of traditional NMs (Krüger et al 2015). Mini-NMs have been operated successfully by several research groups for several years (Poluianov et al. 2015; Usoskin et al. 2015; Heber et al. 2015). Due to their small size and autonomous operation, the mini-NM is ideally suited to be used for latitude scans, which has been done before by Heber et al. (2015) and Krüger et al. (2008).

In this paper we present initial results from a newly re-designed mini-NM, using a  $^3\text{He}$  counting tube, installed on the South African Antarctic research vessel, the SA Agulhas II. This instrument uses a new version of the electronics system described by Strauss et al. 2020. Results from this system, featuring very high temporal resolution, were recently reported by Similia et al. (2020), Strauss et al. (2021) and Strauss et al. (2022)

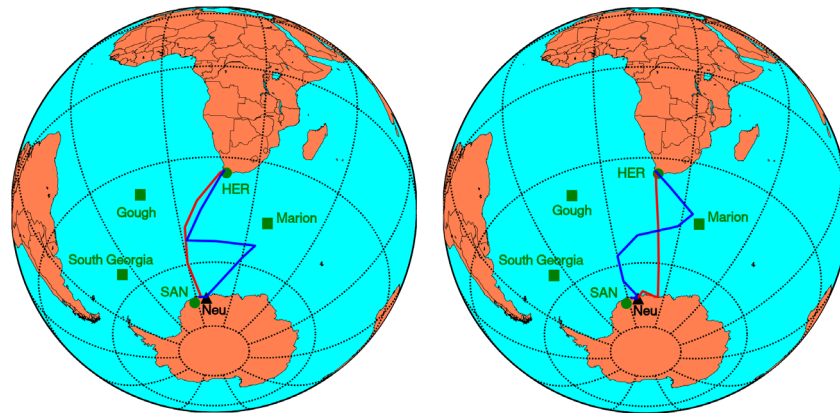


**Fig. 2:** The four latitude scans performed by the SA Agulhas II during the 2019/2020 Antarctic relief voyages. Voyages starting in Cape Town are coloured red.

The redesigned mini-NM was installed on the SA Agulhas II in early December 2019. An unused, and un-heated, storeroom on the upper deck was selected. This region of the ship is circled in the left panel of Fig. 1 which shows the SA Agulhas II anchored at the Fimbul ice shelf in Antarctica, and uploaded materials for the yearly relief voyage to the South African Antarctic base, SANAE IV. The right panel of Fig. 1 shows an image of the monitor, with the newly installed mechanical vibration dampeners circled.

## 2. The 2019/2020 SANAE IV relief voyage

The 2019/2020 Antarctic relief voyage was ideally suited to test the working of the redesigned mini-NM as two voyages were performed; a first relief voyage to the SANAE IV base, and a second to the German Neumayer-Station III. This gives a total of four latitude scans, although not a very wide range of magnetic rigidities were covered. The four latitude scans are illustrated in Fig. 2, with red showing voyages starting in Cape Town. Also shown on the map is the position of the SANAE IV base (SAN), the Hermanus NM (HER), located near Cape Town, Neumayer (Neu), and other regular stops for the SA Agulhas II (South Georgia, Marion, and Gough Islands).

The entire raw data set for the 2019/2020 takeover season is presented in Fig. 3 in minute cadence. The red and green shading indicate different periods; green shading indicates the time when the ship moves between Cape Town harbour and the SANAE ice shelf, while red shading indicated periods when the ship is anchored. The naming convention for these periods are included in the top panel.

## 3. Temperature and pressure corrections

It is well-known that the count rate of an NM depends on the temperature of the instrument, and this has also been confirmed to be the case for the mini-NM (e.g. Moraal et al. 2003; Krüger et al. 2008; Heber et

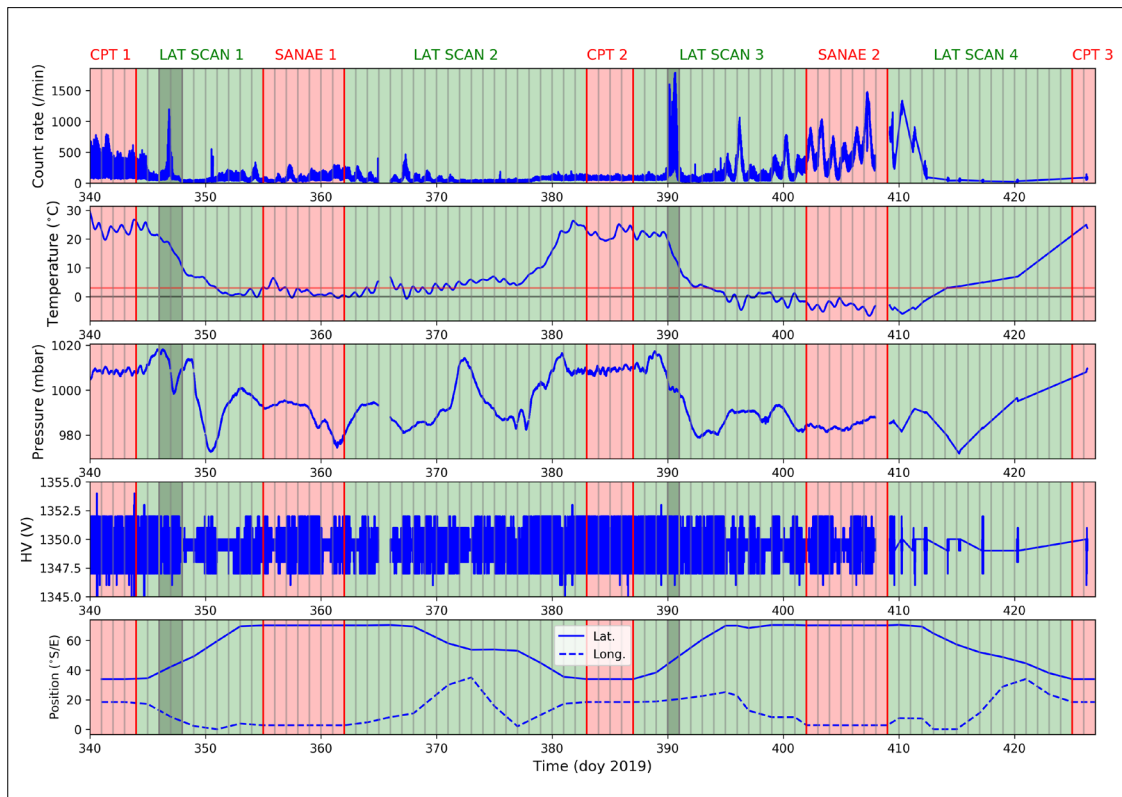


**Fig. 3:** An overview of the mini-NM measurements taken during the 2019/2020 Antarctic relief voyages.

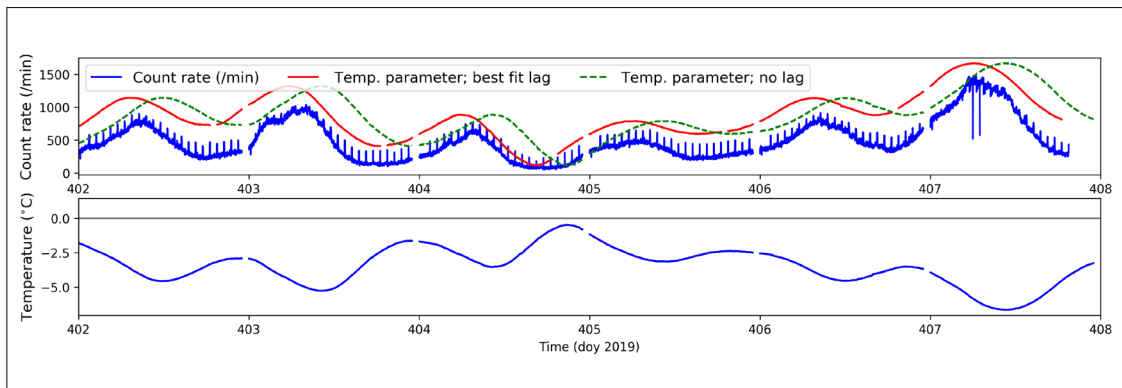


**Fig. 4:** The top panel shows the uncorrected count rate (blue curve) and the absolute temperature (with an offset), referred to as the temperature parameter, uncorrected for any temporal lag effects (green dashed curve) and corrected with the optimized time lag value (red curve). The bottom panel shows the measured temperature.

al. 2015). The temperature dependence of an NM, however, is complex as the different components react differently to temperature variations leading to different absorption and attenuation lengths, and also possibly different neutron production rates (Evenson et al. 2005).

In Fig. 4 we show, in the top panel, the uncorrected (for pressure) count rate for the period 2019 DOY 402 to 2019 DOY 408 the so-called SANAE 2 time period where the ship was anchored at the ice shelf. In the bottom panel, the corresponding temperature is shown, illustrating a definite correlation with the

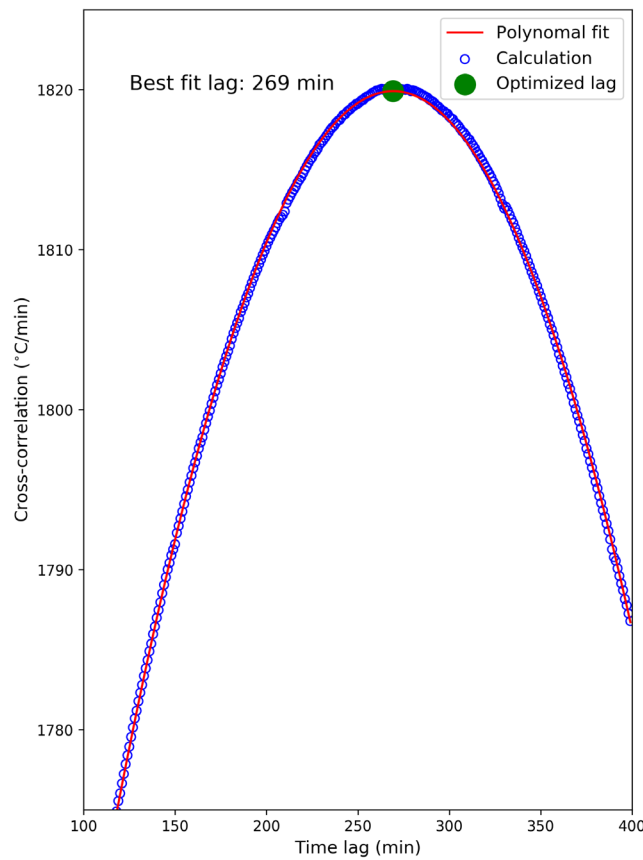


**Fig. 5:** A cross correlation between the temperature and count rate for various temporal lags (blue symbols). A second order polynomial is fitted (red curve) to find the optimal lag value (indicated by the green symbol).

count rate; lower temperatures generally lead to high count rates. The absolute temperature (with an offset for clarity) is shown in the top panel (green dashed curve), illustrating that there is also a lag between the temperature and the count rate. This lag is because of the large thermal mass of the mini-NM and the fact that the temperature probe is inserted against the  $^3\text{He}$  tube (see also the discussion by Evenson et al. 2005).

To correct for this time-lag between the count rate and the temperature, the cross-correlation between these two quantities are calculated for various level of temporal lag, i.e.

$$N * T(n) = \sum_{m=0}^M N(m) \circ T(m + n)$$

where  $N$  and  $T$  are the count rate and temperature time series,  $n$  is the lag (in minutes) and there are  $M$  counts in the series. The results of the cross-correlations analysis are shown as the blue symbols in Fig. 5. There is a maximum correlation at  $\sim 270$  min. To better quantify the magnitude of the lag, a second order polynomial is fitted to the cross-correlation results, and its maximum value is obtained, giving an optimized lag value of 269 min. This time lag is applied to the temperature measurements (which are now shifted 269 min earlier), and the resulting time series is shown as the red curve in the top panel of Fig. 5. This *lag corrected temperature* time series is used for the calculations in the next section.

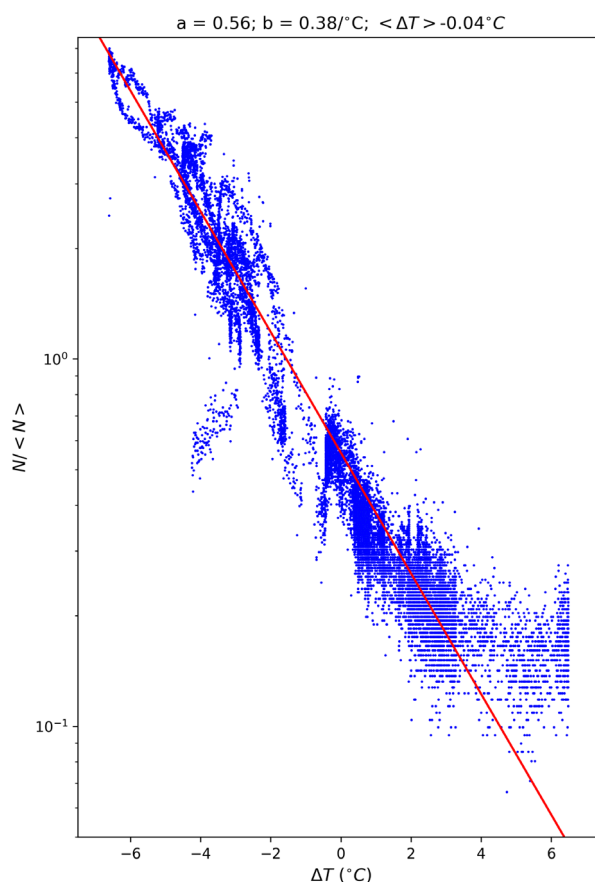


**Fig. 6:** The measured count rate (blue symbols) during the SANAE 2 time interval is well described by an exponential function (red curve).

Now that we have accounted for any lag effects, the temperature dependence of the mini-NM count rate for the SANAE 2 time period can be evaluated. Following the usual approach (e.g. Krüger et al. 2008), an exponential relationship is assumed, where

$$\frac{N}{\langle N \rangle} = a \exp(-\beta_T \Delta T)$$

with  $\Delta T = T - \langle T \rangle$ ,  $\beta_T$  the temperature coefficient,  $a$  is a fit constant, and the angle brackets  $\langle \rangle$  indicating average values. Note that this equation can be approximated by a linear function when either  $\beta_T$  or  $\Delta T$  is small. However, as shown the left panel of Fig. 6, the measurements (blue symbols) during the SANAE 2 time period can be very well described by an exponential regression line (red curve). We find an extremely large temperature coefficient of  $\beta_T \sim 40\%/^{\circ}\text{C}$  which is much larger than the value of  $\beta_T \sim 0.1\%/^{\circ}\text{C}$  from Moraal et al. (2003) and Krüger et al. (2008) for the same monitor (although using older electronics) at ambient temperatures larger than  $\sim 10^{\circ}\text{C}$ . As this very large exponential increase in the count rate below  $\sim 3^{\circ}\text{C}$  is therefore most likely due to noise from the electronics and these data were not used for the rest of the analysis. Further temperature tests in the laboratory confirms that this is an instrumental effect at very low temperatures.

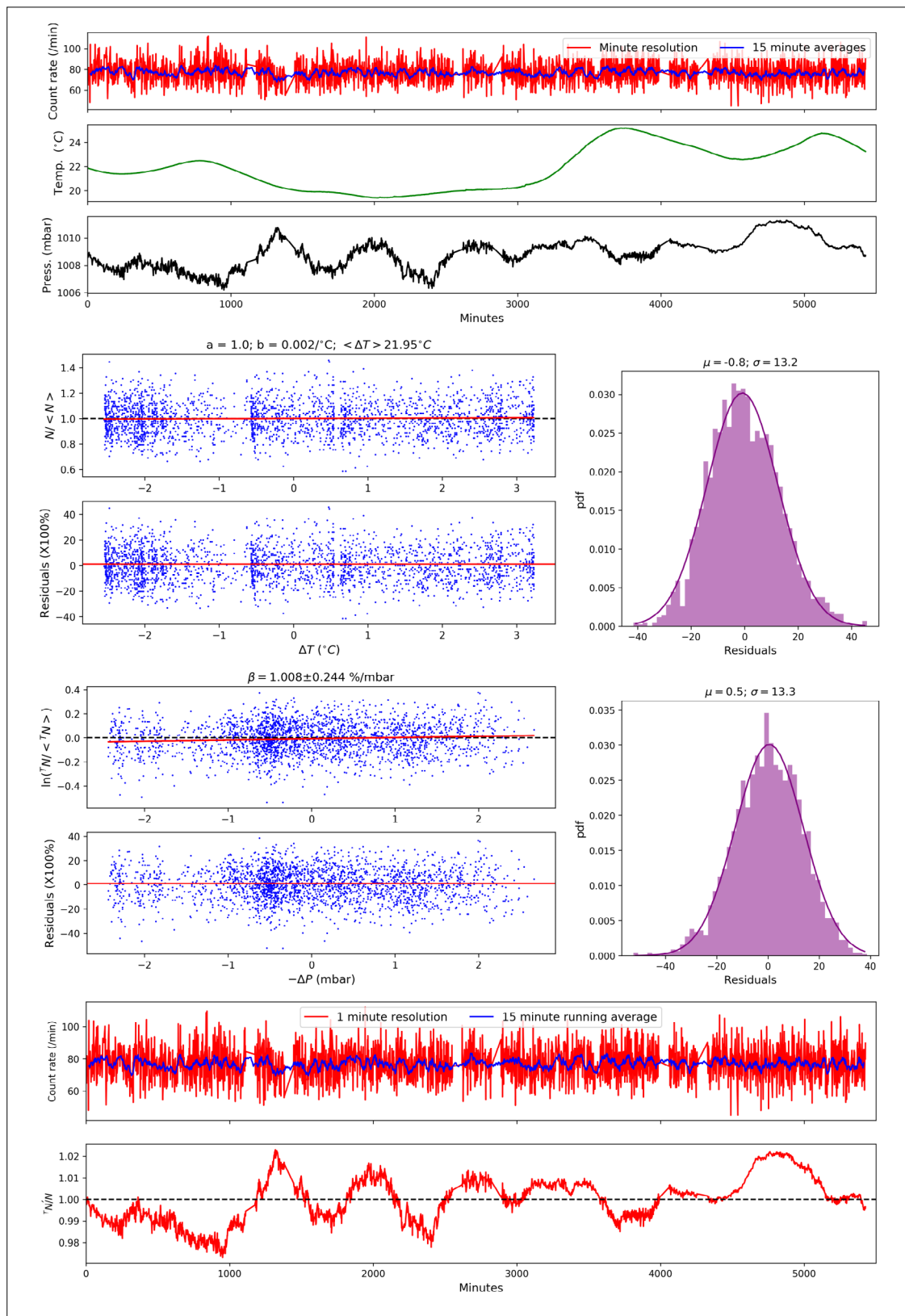


Fig. 7: An example of how the daily measurements were processed, including temperature and pressure correction details.

The following analysis was performed for each day's data. As an example, we show here the data taken during the period labelled CPT 2, i.e. DOY 383 – 387. For these five days the ship was anchored at Cape Town harbour for refueling and loading of cargo. The top panel of Fig. 7 shows the measured count rate, temperature, and pressure in minute resolution. As the temperature varied very little in this interval (and this is in general also true when looking only at daily periods of data), a linear temperature correction is then performed, where

$$\frac{N}{\langle N \rangle} = a - \beta_T \Delta T.$$

Once  $\beta_T$  is known, the temperature-corrected count rate can be calculated, with results shown in the middle panel, where, for this case, the temperature coefficient is  $\sim 0.2\%/^{\circ}\text{C}$ . This value is more in line with previous measurements by Krüger et al. (2008). We also show the residuals of this linear fit, and the distribution of the residuals, in the middle panel. The probability density function (pdf) of the residuals (purple histogram) is fitted by a Gaussian function (purple curve). The mean and variance of the Gaussian function are indicated in the figure's legend.

The temperature-corrected count rate varies as

$$N = \langle N \rangle \exp(-\beta \Delta p)$$

where  $\beta$  is the pressure coefficient and  $\Delta p = P - \langle P \rangle$ . The resulting  $\beta \sim 1\%/mbar$  is indicated in the figure title. Regression residuals are again shown. The bottom panels of Fig. 7 show the pressure and temperature corrected count rate and the uncorrected to corrected count rate ratio.

The analysis discussed in the previous section was repeated for every day of the 2019/2020 relief voyage that produced reliable measurements. I.e., only days with a temperature larger than  $3^{\circ}\text{C}$ . For each such day, the daily average temperature- and pressure-corrected count rate was calculated and compared to the geomagnetic cut-off, calculated from the daily average position of the ship, using the online calculator <http://nearfld.com/util/rigidity.php> (last accessed July 5, 2023). The results of this are presented in the top left panel of Fig. 8 for the three latitude scan. The solid curve is the prediction from Caballero-Lopez and Moraal (2012) using their Eq. (13) with the 1987 sea level (SL) parameters and normalized to  $N_0 = 90$  counts/min. Above  $\sim 2.8\text{GV}$ , the measured latitude profile seems consistent with the expectation and previous results. However, below  $\sim 2.8\text{GV}$ , and shaded gray, there is a clear discrepancy with lower-than-expected NM counts. By also examining the count rate against the latitude of the ship (bottom left panel), it is clear that there is a discrepancy when the ship passes above the  $45^{\circ}\text{S}$  latitude mark. The reason for this discrepancy is presented in the next section.

The top right panel of Fig. 8 shows the calculated pressure coefficient as a function of the geomagnetic cut-off. The vertical dashed line indicates the average value of  $\sim 1.3\%/mbar$ . Given the relatively low count rate of the mini-NM, and the associated large errorbars in  $\beta$ , we did not find any latitude dependence.



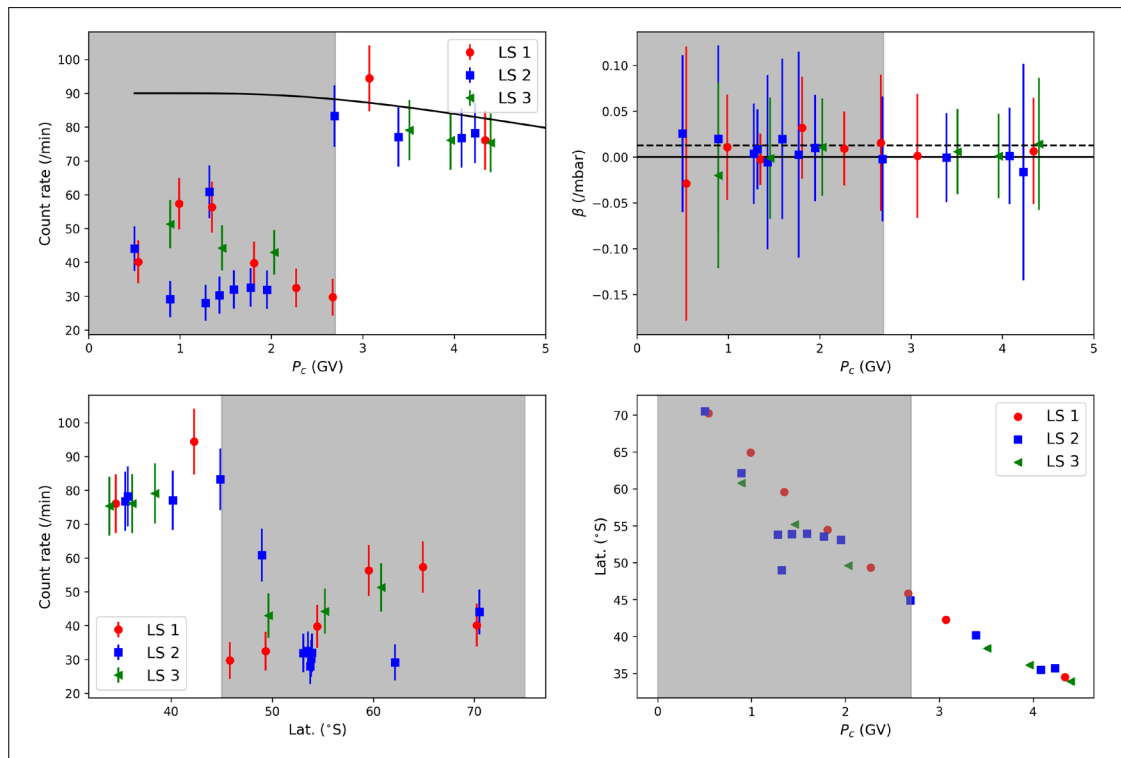


**Fig. 8:** Daily average temperature- and pressure-corrected count rates as a function of geomagnetic cut-off rigidity (top left panel) and latitude (bottom left panel). The cut-off rigidity dependence of the pressure coefficient is presented in the top right panel, and the relationship between the cut-off rigidity and the latitude is in the bottom right panel.

#### 4. Waiting time distribution and high-frequency interference

The outer moderator surrounding the NM blocks thermal particles from entering the detector. In the lead producer, some of the non-thermal atmospheric particles interact with the lead nuclei to form a new low-energy neutron component, so the particle spectrum here consists of two components: The original incident particles that did not undergo any additional reactions and neutrons produced inside the lead producer. These non-thermal distributions now pass through the inner moderator forming a thermal distribution. These thermal neutrons can now be captured by the  $^3\text{He}$  gas during a neutron capture reaction. The protons or alpha particles formed during the capture process are then accelerated, via an applied voltage, towards the positive cathode where they can be counted as a pulse by appropriate electronics. It does, however, also happen that some accelerated particles interact with the walls of the  $^3\text{He}$  tube and deposit some energy there (the so-called *wall effect*, Knoll 2010) so that the recorded neutron distribution appears to have a tail towards lower pulse lengths. However, it is important to note that the recorded pulse width from the NM has no relation to the energy of the incident neutrons: Due to a combination of thermalization by the moderators, and by the nature of the neutron capture process, all information regarding the energy of the incident proton and neutron is lost.

However, low- and high-energy protons interact with the lead producer differently. Low energy protons and neutrons interact with the lead producer, and thus the  $^3\text{He}$  gas, in a random fashion and their observed pulses show a stochastic nature with subsequent pulses unrelated to each other. A high-energy

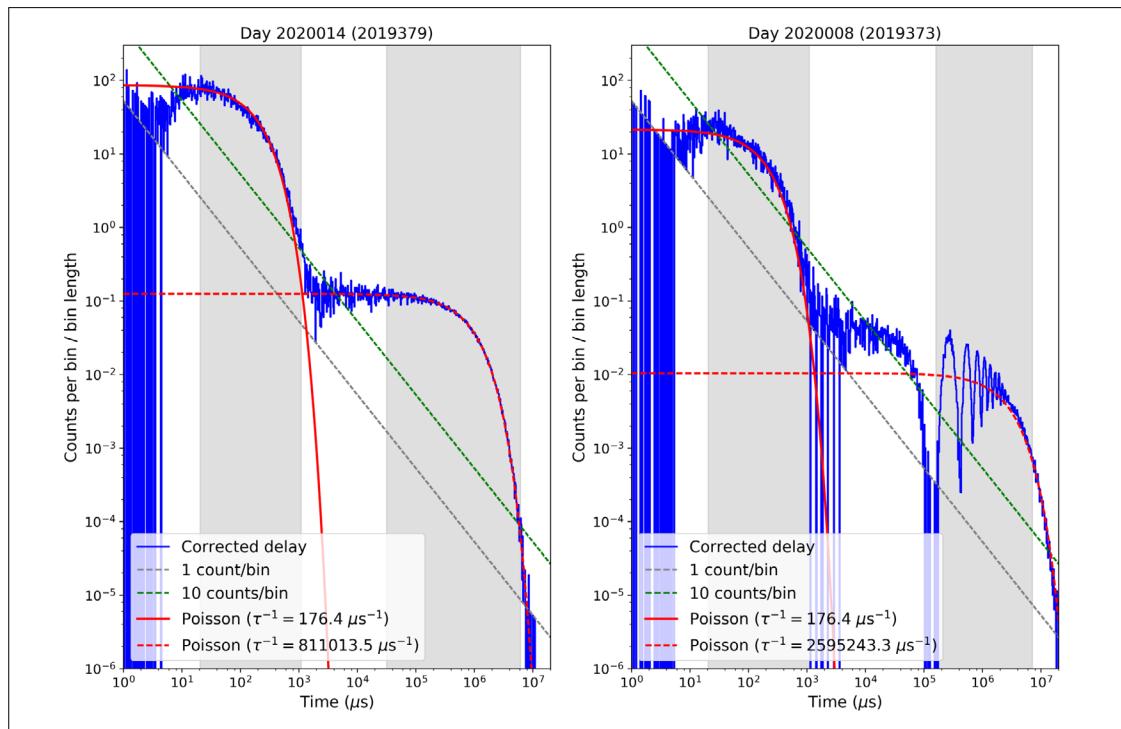


**Fig. 9:** Multiplicity of the observed count rate as measured during two different days. The waiting time distributions are fitted by two Poisson-like distributions, with the fit results indicated in the legend.

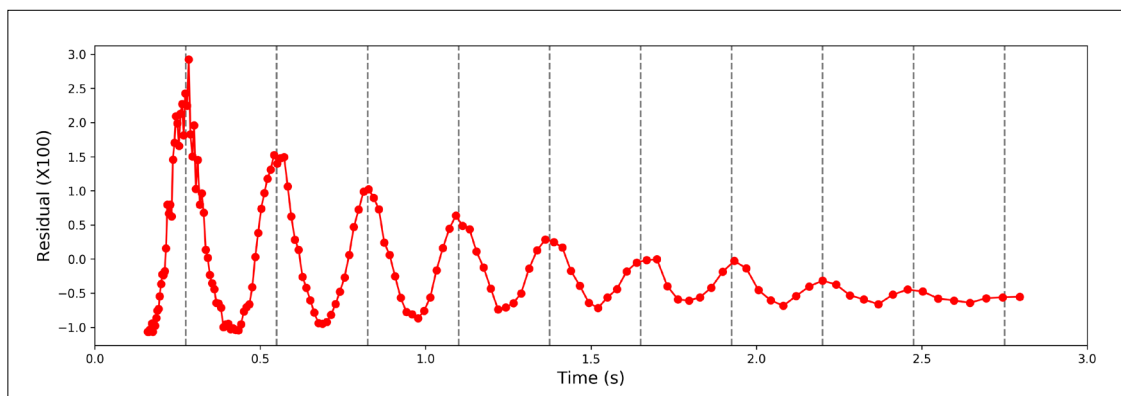


**Fig. 10:** The deviation of the observed waiting time distribution from a fitted Poisson distribution. The vertical dashed lines have a periodicity of 0.275 s.

proton, on the other hand, can interact with the lead nuclei to form a number of low-energy *evaporation neutrons* (e.g. Bieber et al. 2004). These neutrons are observed as several pulses over a short period, showing a high temporal correlation. This is usually expressed in terms of the waiting time distribution (i.e. the time between subsequent pulses observed in the monitor) as the level of multiplicity. Thus, looking at the waiting time distribution, as an indication of the multiplicity, observed by the monitor these two components are clearly distinguishable. By looking at the ratio of these components some information about the incident particle spectrum can be reconstructed (see e.g. Ruffolo et al. 2016; Mangeard et al. 2016; Banglieng et al. 2020).

As discussed in the previous section, a discrepancy in the mini-NM count rate is visible when the ship crosses 45°S in latitude; a deficiency of counts is observed. This coincides with the activation of the ship's ice radar. We, therefore, suspect that the rotating radar dish blocks some of the incoming atmospheric protons and neutrons. Note that the monitor is installed directly below this dish, as shown in Fig. 1. In order to test the blocking hypothesis, we examine the waiting time distribution of the monitor on two different days, 2020008 (2019373) and 2020014 (2019379), using the YEARD0Y notation (year followed by the day-of-year), during latitude scan 2 when the ship was on route to Cape Town harbour. On both days, only minor temperature effects are noticeable and needs to be corrected for. During 2020008, the ship was ~53°S, and on 2020014, it was at ~42°S. The calculated waiting time distribution are shown in Fig. 9 as blue curves. The green and gray dashed lines show the 1 and 10 counts/bin limits. The high multiplicity part of the distribution (i.e., the part with shorter waiting times) forms due to high-energy protons producing multiple neutrons in the lead producer. The low multiplicity part (at longer waiting times) are neutrons and protons that are captured randomly with the counts unrelated. We fit the waiting time distributions with two Poisson-like distributions for each multiplicity component. The results are shown in Fig. 10 as the red curves. The grey-shaded areas indicate the data used to fit each distribution. The spectrum for 2020014, which is during a time when no discrepancies in the data are observed, shows the expected two component Poisson distribution. The spectrum for 2020008, which coincides with a day showing such a discrepancy, shows additional features: The high multiplicity part of the distribution is lower than for 2020014 but interestingly has the same shape. The low multiplicity part, however, shows quasi-periodic decreases in counts. This, at least partially, confirms our suspicion that the radar periodically blocks some of the incident atmospheric protons and neutrons: At fixed time values, there is a deficiency of particles in the low part of the waiting time distribution. However, only of the high multiplicity part of the distribution is reduced (due to the reduced incoming proton/neutron flux) while the shape remains the same, clearly showing that only the incident particles are affected and not the neutrons produced inside the lead producer.

We can further analyse the blocking of incident particles by examining the residuals in the low multiplicity part of the 2020008 distribution (the right panel of Fig. 10). Here, we define the residual as the difference between the measured waiting time distribution and that predicted by the fitted Poisson-like distribution, normalized to the average difference. This quantity is shown, as a function of  $\Delta t$ , in Fig. 10. The vertical dashed lines, corresponding to the different peaks in the residual, are placed every 0.275 s revealing the quasi-periodic behaviour of the inference of incident particles. The overhead ice radar rotates at a rate of 40 rotations-per-minute. As this instruments consists of two rotating fins, we can expect a fin to pass over the monitor every 0.75 s. This is about 3 times the observed signal period. At the moment a direct correlation between the ice radar and the mini-NM cannot be proven. However, as we observe interference only at latitudes greater than ~45°S, with co-insides with the operation of the ice radar system, we still believe the radar system is the main suspect in influencing the operation of the NM.

## 5. Discussion and future outlook

A newly redesigned version of a mini-NM was placed on the SA Agulhas II during its 2019/2020 annual relief voyage between Cape Town, South Africa, and the Antarctic ice shelf near the South African Antarctic base SANAE IV. Four such latitude scans were performed in 2019/2020, giving us a good opportunity

to test several new modifications to the instrument, including new (and much more sensitive) electronics and a redesigned cradle featuring vibration dampeners.

During the SANAE 2 time interval, when the ship was anchored against the ice shelf, the average temperature measured inside the monitor was  $T \sim 0^\circ\text{C}$ . It is found that, during such extremely low temperatures, the mini-NM count rate increases exponentially with a decrease in temperature. An extremely large temperature coefficient of  $\beta_T \sim 40\%/^\circ\text{C}$  is found for such scenarios, which is believed to be caused by noise from the electronics. However, when the temperature of the detector rises above  $\sim 3^\circ\text{C}$ , a small to moderate temperature dependence is found with  $\beta_T \sim 0.2\%/^\circ\text{C}$ , or even smaller. The significant temperature dependence, and hence the corresponding correction needed for periods with temperatures less than  $3^\circ\text{C}$ , introduce large uncertainties into the temperature-corrected count rate and essentially makes these periods unusable for further analysis.

Daily measurements allow us to study the relationship between the count rate and the geomagnetic cut-off. In contrast to what was expected, we measured a decrease in the counting rate below  $\sim 2.7\text{GV}$ . This is, however, not related to the physics of cosmic ray transport through the geomagnetic field, but is rather caused by, presumably, interference from the ship's ice radar which is activated below  $\sim 45^\circ\text{S}$ . We can study this high-frequency interference by looking at the measured waiting time distribution. This allowed us to confirm that incident protons and neutrons are blocked periodically from reaching the detector. In addition, we can determine that this interference occurs with a frequency of  $\sim 3.6\text{Hz}$ . This shows, for the first time, that the multiplicity derived from the NM observations, can be used to test the stability of the mini-NM observations.

Due to both the large temperature effect and the interference from the ice radar at the mini-NM's current position, we are currently looking at moving it to a more suitable location on board the SA Agulhas II. There, hopefully, we will be able to operate the instrument in a continuous fashion for several years.

## Acknowledgements

This work is based on the research supported in part by the National Research Foundation of South Africa. Support from the NRF's South African National Antarctic Programme (SANAP; grant number 110741) is especially acknowledged. Opinions expressed and conclusions arrived at are those of the authors and are not necessarily to be attributed to the NRF. We acknowledge support from the Alexander von Humboldt Foundation's Group Linkage Program.

## References

- Banglieng, C., Janthaloet, H., Ruffolo, D., et al., 2020, Tracking Cosmic-Ray Spectral Variation during 2007 - 2018 Using Neutron Monitor Time-delay Measurements. *Astrophys. J.* 890, 21, <https://doi.org/10.3847/1538-4357/ab6661>
- Bieber, J.W., Clem, J.M., Duldig, M.L., et al. 2004, Latitude survey observations of neutron monitor multiplicity. *J. Geophys. Res.* 109, A12106, <https://doi.org/10.1029/2004JA010493>
- Bütikofer, R., 2018, Solar Particle Radiation Storms Forecasting and Analysis: The HESPERIA HORIZON 2020 Project and Beyond. Ground-Based Measurements of Energetic Particles by Neutron Monitors, ed. by O.E. Malandraki and N.B. Crosby, 95 - 111, Springer International Publishing
- Caballero-Lopez, R.A. and Moraal, H., 2012, Cosmic-ray yield and response functions in the atmosphere. *J. Geophys.*

- Res. 117, A12103, <https://doi.org/10.1029/2012JA017794>
- Caballero-Lopez, R.A., 2015, An estimation of the yield and response functions for the mini neutron monitor. *J. Geophys. Res.* 121, 7461 – 7469, <https://doi.org/10.1002/2016JA022690>
- Clem, J.M. and Dorman, L.I., 2000, Neutron Monitor Response Functions. *Space Sci. Rev.* 93, 335 – 359, <https://doi.org/10.1023/A:1026508915269>
- Evenson, P., Bieber, J.W., Clem, J., et al. 2005, Neutron Monitor Temperature Coefficients: Measurements for BF<sub>3</sub> and <sup>3</sup>He Counter Tubes. *Proceedings of the 29th International Cosmic Ray Conference*, 2, 485
- Heber, B., Galsdorf, D., Gieseler, J., et al. 2015, Mini neutron monitor measurements at the Neumayer III station and on the German research vessel Polarstern. *Proceedings of the 34th International Cosmic Ray Conference*, 34, 122
- Knoll, G.F., 2010, *Radiation Detection and Measurement*, 4th ed. Wiley, New Jersey
- Krüger, H., Moraal, H., Bieber, J.W., et al. 2003, First Results of a Mobile Neutron Monitor to Intercalibrate the Worldwide Network. *Proceedings of the 28th International Cosmic Ray Conference*, 6, 3441
- Krüger, H., Moraal, H., Bieber, J.W., et al. 2008, A calibration neutron monitor: Energy response and instrumental temperature sensitivity. *J. Geophys. Res.* 113, A08101, <https://doi.org/10.1029/2008JA013229>
- Krüger, H., Moraal, H., Nel, R. et al. 2015, The mini neutron monitor programme. *Proceedings of the 34th International Cosmic Ray Conference*, 34, 223
- Mangeard, P.-S., Ruffolo, D., Saiz, A., et al., 2016, Dependence of the neutron monitor count rate and time delay distribution on the rigidity spectrum of primary cosmic rays. *J. Geophys. Res.* 121, 11620 – 11,636, <https://doi.org/10.1002/2016JA023515>
- Moraal, H., Benadie, A., de Villiers, D., et al. 2001, A mobile neutron monitor to intercalibrate the worldwide network. *Proceedings of the 27th International Cosmic Ray Conference*, 10, 4083
- Moraal, H., Kruger, H., Benadie, A., et al. 2003, Calibration of the Sanae and Hermanus Neutron Monitors. *Proceedings of the 28th International Cosmic Ray Conference*, 6, 3453
- Poluianov, S., Usoskin, I., Mishev, A., et al. 2015, Mini Neutron Monitors at Concordia Research Station, Central Antarctica. *J. Astron. and Space Sci.* 32, 281 – 287, <https://doi.org/10.5140/JASS.2015.32.4.281>
- Ruffolo, D., Saiz, A., Mangeard, P.-S., et al. 2016, Monitoring Short-term Cosmic-ray Spectral Variations Using Neutron Monitor Time-delay Measurements. *Astrophys. J.* 817, 38, <https://doi.org/10.3847/0004-637X/817/1/38>
- Simila, M., Usoskin, I., Poluianov, S., et al. 2021, High-altitude polar NM with the new DAQ system as a tool to study details of the cosmic-ray induced nucleonic cascade. *J. Geophys. Res.* 126, e2020JA028959, <https://doi.org/10.1029/2020JA028959>
- Simpson, J.A., 2000, The Cosmic Ray Nucleonic Component: The Invention and Scientific Uses of the Neutron Monitor. *Space Sci. Rev.* 93, 11 – 32, <https://doi.org/10.1023/A:1026567706183>
- Strauss, R.D., Poluianov, S., van der Merwe, C., et al., 2021, The mini-neutron monitor: a new approach in neutron monitor design. *J. Space Weather and Space Climate*, 10, 39, <https://doi.org/10.1051/swsc/2020038>
- Strauss, R.D., van der Merwe, C., Diedericks, C., et al. 2021, The updated SANAe neutron monitor. *Adv. Space Res.*, 68, 2661 – 2675, <https://doi.org/10.1051/swsc/2020038>
- Strauss, R.D., Giday, N.M., Seba, E.B., et al. 2022, First results from the ENTOTO neutron monitor: Quantifying the waiting time distribution. *Adv. Space Res.*, in press
- Usoskin, I., Poluianov, S., Moraal, H., et al., 2015, A mini neutron monitor in Central Antarctica (Dome Concordia). *Proceedings to the 34th International Cosmic Ray Conference*, 34, 217

## Open Access

This paper is published under the Creative Commons Attribution 4.0 International license (<https://creativecommons.org/licenses/by/4.0/>). Please note that individual, appropriately marked parts of the paper may be excluded from the license mentioned or may be subject to other copyright conditions. If such third party material is not under the Creative Commons license, any copying, editing or public reproduction is only permitted with the prior consent of the respective copyright owner or on the basis of relevant legal authorization regulations.